J. Fluid Mech. (2002), *vol.* 470, *pp.* 383–410.
DOI: 10.1017/S0022112002001568 Printed in the United Kingdom

Three-dimensional nonlinear solitary waves in shallow water generated by an advancing disturbance

By YILE LI AND PAUL D. SCLAVOUNOS

Department of Ocean Engineering, Massachusetts Institute of Technology, Cambridge, MA 02139, USA

(Received 13 November 2001 and in revised form 12 April 2002)

The nonlinear long waves generated by a disturbance moving at subcritical, critical and supercritical speed in unbounded shallow water are investigated. The problem is formulated by a new modified generalized Boussinesq equation and solved numerically by an implicit finite-difference algorithm. Three-dimensional upstream solitary waves with significant amplitude are generated with a periodicity by a pressure distribution or slender strut advancing on the free surface. The crestlines of these solitons are almost perfect parabolas with decreasing curvature with respect to time. Behind the disturbance, a complicated, divergent Kelvin-like wave pattern is formed. It is found that, unlike the wave breaking phenomena in a narrow channel at $F_h \geqslant 1.2$, the three-dimensional upstream solitons form several parabolic water humps and are blocked ahead of the disturbance at supercritical speed in an unbounded domain for large time.

1. Introduction

In waterways around the world, high-speed vessels are used widely as a fast means of transportation. A large-amplitude wake wash generated by those fast ships and propagating shoreward has become an issue of central concern for coastal communities. The large waves have a significant impact on the safety of people, property and craft, and are responsible for the erosion of coastlines and sea bottoms and the biological environment. In a fatal accident which occurred in Harwich, a port on England's east coast, in July 1999, one surviving victim reported that the wave looked like 'the white cliffs of Dover' (see Hamer 1999). Research carried out in Europe shows that the soliton produced by a fast ferry was probably responsible for the disaster.

In restricted waters, solitary waves can be generated ahead of the ship bow, propagating upstream keeping their shape and velocity constant. Scott Russel first discovered this phenomenon in 1834 as he watched a canal boat pulled by horses stopping suddenly. In ship hydrodynamics, it has been observed (see Thews & Landweber 1935, 1936) in a towing tank that a ship model advancing steadily can radiate waves upstream that move faster than the ship and a steady state of the wave resistance cannot be reached. The extensive experimental, theoretical and numerical investigations of this type of wave were pioneered by the systematic experiments of Huang *et al.* (1982) for ship models moving at various transcritical speeds. Investigating extensive experimental results for a Series 60 ship model, Ertekin, Webster & Wehausen (1984) pointed out that the blockage coefficient A/Wh (A is the maximum cross-sectional

area of the ship, W is the width and h the depth of the channel) is the dominant parameter for the generation of solitons.

Wu & Wu (1982) presented numerical computations for the nonlinear long waves forced by a moving pressure patch in the vicinity of the critical speed $U = \sqrt{gH}$ in a two-dimensional tank, based on a generalized Boussinesq (gB) model (see Wu 1981) assuming a balance between nonlinear and dispersive effects. It was shown that a solitary wave first emerges ahead of the disturbance, and finally propagates upstream. Starting from the linear solution, Akylas (1984) and Cole (1985) developed the nonlinear theory which accounts for the finite-amplitude effects and found that the generated waves are governed by a forced Korteweg–de Vries (fKdV) equation. Ertekin *et al.* (1984) carried out a numerical calculation by using the Green–Naghdi fluid sheet equations. The forcing is taken as a pressure distribution on the free surface or the underwater topography and a similar phenomenon is reported: a succession of upstream-running solitons are generated periodically ahead of the disturbance, while a weakly nonlinear and dispersive wave train develops downstream of an elongated depressed water surface, trailing the disturbance. Wu (1987) presented a preliminary study of the underlying basic mechanism of the phenomenon by analysing the stability of the solutions of the fKdV equation. In a joint numerical and experimental study, Lee, Yates & Wu (1989) found that both the gB and fKdV models obtain qualitatively similar predictions of the phenomenon of the precursor solitons, showing a satisfactory agreement with experiments. Casciola & Landrini (1996) used an accurate boundary integral approach to simulate the flow and carried out a detailed comparison between the fully nonlinear model, and gB and fKdV models. Zhang & Chwang (1999) investigated the influence of viscous effects on a two-dimensional submerged body moving at transcritical speed by solving the Navier–Stokes equations with the complete set of no-slip boundary conditions numerically.

In a restricted channel of shallow water, the two-dimensional upstream solitons are generated by a disturbance with a three-dimensional geometry at a transcritical speed. Mei (1986) derived a one-dimensional inhomogeneous KdV equation for the flow around thin bodies extending throughout the water depth. The corresponding result is two dimensional for both upstream and downstream waves if the channel width is small: $W \ll h^2/a$, a being the typical wave amplitude. Ertekin, Webster & Wehausen (1986) used the restricted Green–Naghdi theory of fluid sheets to perform the three-dimensional calculation of waves generated by an impulsively started pressure patch travelling at the transcritical speed. The two-dimensional solitons propagate upstream periodically, whereas a three-dimensional doubly corrugated set of waves is formed behind the disturbance. By analysing the linear dispersive relation near the critical speed, Katsis & Akylas (1987) derived a forced nonlinear Kadomtsev–Petviashvili (KP) equation to describe the linear dispersive, nonlinear and transverse effects governing the nonlinear long waves excited by a moving pressure distribution. The sidewall is not essential for the radiation of upstream waves but is for the transformation of curved waves to straight-crested solitons. Pedersen (1988) studied the wave patterns generated by a pressure field, source distribution and bottom topography in wide channels based on the Boussinesq equations. The formation of two-dimensional solitons is related to the Mach reflection at the sidewall of the channel. Other researchers solved the Laplace equation with the exact free surface condition numerically. Bai, Kim & Kim (1989) and Choi *et al.* (1990) studied the nonlinear free surface flow produced by a three dimensional ship hull by means of the finite element method.

From the viewpoint of applications, the real ship geometry has to be considered for the demands of high-speed vessel design. Using the matched asymptotic expansion method, Choi & Mei (1989) obtained the homogeneous KP equation with flux conditions on the symmetric plane under the assumption of a slender body. The normal condition of wave elevation is related to the second x-derivative of the longitudinal sectional area. Chen & Sharma (1995) extended that method and took the local wave elevation and longitudinal disturbance velocity into account. The wave force, hydrodynamic lift force and trim moment are calculated for the fixed-hull case and sinkage and trim are calculated for the free-hull case.

It is natural to ask if there exists a steady state or what the unsteady state looks like for a disturbance moving at the critical speed of a long wave in horizontally unbounded domain, in which the blockage parameter tends to zero. Katsis & Akylas (1987) first dealt with this problem using the forced KP equation and a nonlinear curved wave emerges in front of the disturbance at the critical condition. They suggested that no nonlinear steady state could be reached in that case. Pedersen (1988) applied a radiation condition at the open seaward boundary and simulated the problem for a sufficiently long time. He suggested that there always exists a stationary state in unbounded sea and the wave pattern is extended some distance ahead of the disturbance when the depth Froude number is close to unity. This might not be true, however, as the following studies presented opposite predictions. Lee & Grimshaw (1990) also employed the KP equation and reported various characteristics of upstream-advancing waves in open sea. A similarity solution was presented under the assumption that the amplitude is constant along the isophasal line of the leading three dimensional soliton. The solitary wave amplitude diminishes in a manner proportional to $O(t^{-2/3})$ and the crestline, which is a parabola, decreases its curvature as it moves. Choi *et al.* (1990) reported the numerical results for a pressure distribution travelling at the critical speed in an open domain and found that the crestline of the leading soliton fits well with a parabola when the upstream wave develops.

The principal focus of the present study is on the three-dimensional upstream solitary waves generated by a moving disturbance at subcritical, critical and supercritical speeds in unbounded shallow water. In § 2, a modified generalized Boussinesq (mgB) equation is derived in terms of the depth-averaged velocity potential and water elevation. No specific limitation is imposed on the scale of the transverse variation and time, hence allowing the modelling of unsteady shallow water waves forced by either a pressure patch on the free surface or a source distribution underwater. The numerical method based on an implicit finite-difference algorithm is described in § 3. An open boundary condition is enforced on both the downstream and open seaward boundaries to allow the wave to propagate outward without reflection. The numerical results and discussion of the solitary waves generated by a pressure distribution and a slender strut are presented in § 4. Conclusions are presented in § 5.

It is found that the crestlines of the upstream long waves generated by the disturbance are nearly perfect parabolas with curvature diminishing as the waves move forward. The phase velocity of the leading soliton is proportional to its amplitude, which decays at a rate of $O(t^{-1/3})$. These properties are independent of the type of disturbance, magnitude and shape of forcing. At supercritical speeds, the upstream solitons are blocked in front of the disturbance without further variation of their amplitude and curvature and move at the same velocity as the disturbance. A steady state will be eventually reached for the supercritical case.

2. Formulation

2.1. *Modified generalized Boussinesq equation*

Let a pressure distribution advance at the constant speed U acting on the surface of a layer of water with uniform depth h. The disturbance is stationary in a reference coordinate system moving with the pressure. Oz points upward and the (x, y)-plane lies on the undisturbed free surface. In this reference frame, a steady current is moving in the positive x-direction with a speed U. Under the assumption of incompressible, inviscid and irrotational flow, the water wave motion is described by the velocity potential $\Phi(x, y, z, t)$ and the free-surface water elevation $\zeta(x, y, t)$.

In this reference frame, the velocity potential $\Phi(x, y, z, t)$ can be decomposed as

$$\Phi(x, y, z, t) = \phi(x, y, z, t) + Ux, \tag{2.1}$$

in which $\phi(x, y, z, t)$ is the disturbance velocity potential representing the flow motion induced by the external disturbances such as the pressure distribution on the free surface, floating bodies or underwater topography.

The velocity potential $\phi(x, y, z, t)$ satisfies the Laplace equation

$$\phi_{xx} + \phi_{yy} + \phi_{zz} = 0. \tag{2.2}$$

The dynamic and kinetic free-surface conditions are

$$\phi_t + U\phi_x + g\zeta + \tfrac{1}{2}\nabla\phi \cdot \nabla\phi + \frac{p}{\rho} = 0 \quad \text{at} \quad z = \zeta, \tag{2.3}$$

$$\zeta_t + U\zeta_x + \phi_x\zeta_x + \phi_y\zeta_y = \phi_z \quad \text{at} \quad z = \zeta. \tag{2.4}$$

On the bottom the non-flux boundary condition is

$$\phi_z = 0 \quad \text{at} \quad z = -h, \tag{2.5}$$

where g is the gravitational acceleration, ρ is the fluid density and p is the forcing pressure on the free surface.

We choose the typical wave amplitude as a, the characteristic wavenumber as k, the characteristic horizontal velocity as $\sqrt{gh}$ and vertical scale as h. The above variables are thus normalized as follows:

$$(x, y) = \frac{(x', y')}{k}, \quad \zeta = a\zeta', \quad z = hz',$$

$$\phi = \frac{\phi' a}{k}\sqrt{\frac{g}{h}}, \quad t = \frac{t'}{k\sqrt{gh}}, \quad p = \rho g a p'.$$

Three dominant parameters are

$$\epsilon = \frac{a}{h}, \quad \mu = kh, \quad F_h = \frac{U}{\sqrt{gh}},$$

in which F_h is the so-called depth Froude number. The Boussinesq approximation is adopted which assumes that ϵ is of the same order as μ^2, which indicates the balance between the nonlinear and dispersive effects for nonlinear long waves.

In terms of these dimensionless variables, (2.2), (2.3), (2.3) and (2.5) become

$$\mu^2(\phi'_{x'x'} + \phi'_{y'y'}) + \phi'_{z'z'} = 0 \tag{2.6}$$

$$\phi'_{t'} + F_h\phi'_{x'} + \zeta' + \tfrac{\epsilon}{2}\left(\phi'^2_{x'} + \phi'^2_{y'} + \frac{\phi'^2_{z'}}{\mu^2}\right) + p' = 0 \quad \text{at} \quad z' = \epsilon\zeta', \tag{2.7}$$

$$\zeta'_{t'} + F_h\zeta'_{x'} + \epsilon(\phi'_{x'}\zeta'_{x'} + \phi'_{y'}\zeta'_{y'}) = \frac{\phi'_{z'}}{\mu^2} \quad \text{at} \quad z' = \epsilon\zeta', \tag{2.8}$$

$$\phi'_{z'} = 0 \quad \text{at} \quad z' = -1. \tag{2.9}$$

Hereafter, we drop primes from (2.6) to (2.9) for brevity.

The velocity potential $\phi(x, y, z, t)$ is assumed analytic and we can expand it in power series with respect to the vertical coordinate about $z = -1$:

$$\phi(x, y, z, t) = \sum_{n=0}^{\infty}(z+1)^n\phi_n(x, y, t). \tag{2.10}$$

Substituting (2.10) into the governing equation (2.6), we obtain

$$\mu^2(\phi_{xx} + \phi_{yy}) + \phi_{zz} = \sum_{n=0}^{\infty}(z+1)^n((n+1)(n+2)\phi_{n+2} + \mu^2\nabla^2\phi_n) = 0, \tag{2.11}$$

where the operator ∇ denotes the gradient in the horizontal plane, i.e. $\nabla = ((\partial/\partial x)\boldsymbol{i} + (\partial/\partial y)\boldsymbol{j})$. The value of z is arbitrary in the range $[-1, \epsilon\zeta]$ and the coefficients of the power of $z+1$ must vanish to satisfy (2.11); thus we obtain

$$(n+1)(n+2)\phi_{n+2} + \mu^2\nabla^2\phi_n = 0, \quad n = 0, 1, 2, \ldots . \tag{2.12}$$

Substituting (2.10) into the sea bottom boundary condition (2.9), we get

$$\phi_z = \phi_1 = 0 \quad \text{at} \quad z = -1. \tag{2.13}$$

From the recursive relation (2.12), the velocity potential components with odd subscripts all vanish,

$$\phi_1 = \phi_3 = \cdots = \phi_{2m+1} = \cdots = 0, \quad m = 0, 1, \ldots . \tag{2.14}$$

In accordance with (2.12), the velocity components of even order can be expressed by the zero-order term ϕ_0 as follows:

$$\begin{aligned}\phi_{2m} &= -\frac{\mu^2}{2m(2m-1)}\nabla^2\phi_{2m-2} \\ &= (-1)^n\frac{\mu^{2m}}{(2m)!}\underbrace{\nabla^2\nabla^2\cdots\nabla^2}_{m}\phi_0, \quad m = 1, 2, \ldots .\end{aligned} \tag{2.15}$$

Consequently the velocity potential can be expressed as

$$\phi(x, y, z, t) = \phi_0 - \frac{\mu^2}{2}(z+1)^2\nabla^2\phi_0 + \frac{\mu^2}{24}(z+1)^4\nabla^2\nabla^2\phi_0 + O(\mu^6) \tag{2.16}$$

with an $O(\mu^6)$ error.

We introduce a depth-averaged velocity potential, defined by

$$\bar{\phi}(x, y, t) = \frac{1}{1+\epsilon\zeta}\int_{-1}^{\epsilon\zeta}\phi(x, y, z, t)\,\mathrm{d}z = \phi_0 - \frac{\mu^2(1+\epsilon\zeta)^2}{6}\nabla^2\phi_0 + O(\mu^4) \tag{2.17}$$

and thus

$$\phi_0(x, y, t) = \bar{\phi}(x, y, t) + \frac{\mu^2H^2}{6}\nabla^2\bar{\phi}(x, y, t) + O(\mu^4), \tag{2.18}$$

where $H = 1 + \epsilon\zeta$.

Substituting (2.18) into (2.16), the three dimensional velocity potential describing

the water wave motion in shallow water is expressed by the velocity potential which is averaged along the vertical coordinate up to an error of $O(\mu^6)$, or

$$\phi(x,y,z,t) = \bar{\phi} + \mu^2\left(\frac{H^2}{6} - \frac{(z+1)^2}{2}\right)\nabla^2\bar{\phi} \\ -\mu^4\left(\frac{(z+1)^2}{12}\nabla^2(H^2\nabla^2\bar{\phi}) - \frac{(z+1)^4}{24}\nabla^2\nabla^2\bar{\phi}\right) + O(\mu^6). \quad (2.19)$$

To account for the coupled nonlinear and dispersive effects for shallow water waves, the dimensionless variable ϵ, representing nonlinearity, and μ, representing dispersion, are assumed to be related as follows:

$$\epsilon = O(\mu^2). \quad (2.20)$$

The order of the time derivative and of transverse derivative of $\bar{\phi}$ and ζ are crucial to the formulation of the problem. Many previous studies showed that the first-order time derivative is of $O(\mu^2)$, and the first-order transverse derivative of $O(\mu)$ (Katsis & Akylas 1987) in a channel of finite width or $O(\mu^{1/2})$ (Mei 1986) in a narrow channel. For the three-dimensional nonlinear long waves generated by a moving disturbance, the evolution of upstream-running waves is transient and three-dimensional. It is difficult to determine the characteristic transverse scale and the time scale explicitly due to the variation of the wave as it develops. Meanwhile, the upstream wave systems are supposed to exhibit different properties from those downstream wave trains, whose counterpart is the Kelvin wake in classical linear theory. To explore the physics of both the precursor waves and the downstream Kelvin-like waves, we assume that the primary time variable is slow and such that

$$\epsilon^2 < O\left(\frac{\partial}{\partial t}\right) < 1.$$

Any combination of a time derivative of $O(\epsilon)$ or $O(\mu^2)$ is omitted to leading order, or

$$O\left(\epsilon\frac{\partial}{\partial t}\right) \ll O(\epsilon), \quad O\left(\mu^2\frac{\partial}{\partial t}\right) \ll O(\mu^2).$$

Following the above assumption, the substitution of (2.19) into the free-surface condition (2.7) leads to

$$\bar{\phi}_t + F_h\bar{\phi}_x = -\zeta + \frac{\mu^2}{3}F_h\nabla^2\bar{\phi}_x - \frac{\epsilon}{2}(\bar{\phi}_x^2 + \bar{\phi}_y^2) - p, \quad (2.21)$$

in which terms of order higher than $O(\epsilon, \mu^2)$ have been omitted.

Hence, (2.8) can be rewritten as

$$\zeta_t + F_h\zeta_x = -\nabla\cdot((1+\epsilon\zeta)\nabla\bar{\phi}) + O(\mu^4). \quad (2.22)$$

The above equation (2.22) is valid for any arbitrary ϵ. Equations (2.21) and (2.22) are the expressions for the generalised Boussinesq (gB) equation (Wu 1981) in the frame moving with a two-dimensional pressure patch on the free surface of shallow water of uniform depth.

The free-surface elevation ζ can be expressed in terms of $\bar{\phi}$ explicitly according to (2.21):

$$\zeta = -\bar{\phi}_t - F_h\bar{\phi}_x + \frac{\mu^2}{3}F_h\nabla^2\bar{\phi}_x - \frac{\epsilon}{2}(\bar{\phi}_x^2 + \bar{\phi}_y^2) - p. \quad (2.23)$$

Rewrite the nonlinear term $\nabla \cdot (\epsilon\zeta\nabla\bar{\phi})$ in (2.22) by substituting (2.23) for the free-surface elevation ζ and omit all terms of order higher than $O(\epsilon, \mu^2)$; we obtain a new form of long-wave model in which all nonlinear terms are expressed by the derivatives of $\bar{\phi}$ uniquely. Eventually, the so-called modified generalized Boussinesq (mgB) equations are obtained by combining with (2.21):

$$\bar{\phi}_t + F_h\bar{\phi}_x = -\zeta + \frac{\mu^2}{3}F_h\nabla^2\bar{\phi}_x - \frac{\epsilon}{2}(\bar{\phi}_x^2 + \bar{\phi}_y^2) - p, \tag{2.24}$$

$$\zeta_t + F_h\zeta_x = -\nabla^2\bar{\phi} + \epsilon F_h(2\bar{\phi}_x\bar{\phi}_{xx} + \bar{\phi}_x\bar{\phi}_{yy} + \bar{\phi}_y\bar{\phi}_{xy}) + \epsilon\nabla \cdot (p\nabla\bar{\phi}). \tag{2.25}$$

Compared with Wu's gB equations (2.21), (2.22), the mgB equations omit some terms of higher order. To $O(\epsilon, \mu^2)$, they are equivalent. However, the latter has some advantages in the implementing of the numerical algorithm which will be described in the following section.

The principal forcing term for the generation of nonlinear long waves due to the applied pressure distribution is p on the right-hand side of (2.24). Since the pressure distribution that we choose to employ is somewhat arbitrary, the last term involving the pressure on the right-hand side of (2.25) is $O(\epsilon)$ and we omit it in the computations.

2.2. *Boundary conditions*

On the ship hull, the fluid particles cannot penetrate the solid body surface. Therefore, the normal component of the flow velocity is equal to the corresponding normal velocity of the rigid hull:

$$\frac{\partial\phi(x, y, z, t)}{\partial n} = -Un_x \quad (x, y, z) \in S_B, \tag{2.26}$$

where S_B is the submerged ship surface and $\boldsymbol{n}(x, y, z)$ is the normal vector at (x, y, z), pointing out of the fluid domain.

Assume that the geometry of the ship hull is expressed in the form

$$y = Y(x, z) = BY\left(\frac{x}{L}, \frac{z}{d}\right) = BY(X, Z),$$

where B, L, d are the half beam-width, half ship length and the draught of the ship respectively. X, Y, Z are the dimensionless variables normalized by L, B, d respectively.

Following the same procedure of non-dimensionalization as in § 2.1, the non-dimensional form of the boundary condition on the ship hull is

$$\phi_y - \frac{1}{\mu}\frac{B}{d}Y_Z\phi_z = \frac{1}{\epsilon}\frac{B}{L}Y_X(F_h + \epsilon\phi_x) \quad \text{at} \quad y = \mu\frac{B}{h}Y(X, Z). \tag{2.27}$$

From (2.16), it is easy to find that the vertical velocity component is a high-order variable compared with the corresponding components in horizontal directions:

$$O(\phi_z) = \mu O(\phi_x, \phi_y).$$

We assume that the ship geometry is thin and its characteristic parameters satisfy

$$\frac{B}{L} = O(\epsilon), \quad \frac{B}{d} = O(\mu), \quad \frac{B}{h} = O(\mu).$$

By expanding (2.27) about the symmetric plane $y = 0$, we can obtain its leading-order term:

$$\phi_y = \frac{F_h}{\epsilon}\frac{B}{L}Y_X \quad \text{at} \quad y = 0. \tag{2.28}$$

Thus the non-flux boundary condition on the ship hull is simplified into a Neumann condition on $y = 0$, which is convenient for both theoretical analysis and numerical calculation.

Taking the average with respect to the vertical variable z from -1 to the free surface $\epsilon\zeta$ for (2.28), we obtain

$$\bar{\phi}_y = \frac{F_h}{\epsilon}\frac{B}{L}\frac{1}{1+\epsilon\zeta}\int_{-1}^{\epsilon\zeta} Y_X \,\mathrm{d}z = \frac{F_h}{2\epsilon}\overline{S}_x + O(\epsilon), \tag{2.29}$$

where $\overline{S}_x$ is the x-derivative of the non-dimensional cross-sectional area of the ship hull under the still water line:

$$\overline{S}_x = \frac{2B}{L}\int_{-1}^{0} Y_X \,\mathrm{d}z. \tag{2.30}$$

The present problem is treated as an initial boundary value problem. Waves propagate away from the disturbance and are subject to the radiation condition that they vanish at infinity:

$$\phi \to 0, \quad \zeta \to 0 \quad \text{as} \quad \sqrt{x^2+y^2} \to +\infty. \tag{2.31}$$

In numerical calculations, the computational field is truncated at some distance away from the disturbance in both the longitudinal and transverse directions. In general, waves can reflect from the truncated boundaries and contaminate the flow in the computational domain. Special care should be taken to implement suitable open boundary conditions to make the waves pass through the boundaries without reflection.

3. Numerical algorithm

3.1. *Finite difference scheme*

A number of finite difference schemes have been presented to solve the KdV or KP equations. Several were proposed by Taha & Ablowitz (1984) for the numerical solutions of the KdV equation. Wu & Wu (1982) employed the modified Euler method to solve the two-dimensional generalized Boussinesq equations. For the three dimensional case, Katsis & Akylas (1987) developed an explicit scheme for the governing equation which results from integrating the KP equation once with respect to x from negative infinity to x. The same method was also applied by Choi & Mei (1989) to study a slender ship moving in restricted water. The drawback of the explicit scheme is that the time step Δt is of order Δx^3, in which Δx is the spatial step, which would result in rapid increase of computation time for the simulation with refined spatial meshes. Chen & Sharma (1995) developed a more efficient numerical technique using the fractional step algorithm with Crank–Nicolson-like schemes in each half-step. In this paper, we develop an implicit finite difference algorithm to solve the mgB equations (2.24) and (2.25).

The unknown $\bar{\phi}$ and ζ on the grid $(i\Delta x, j\Delta y)$ in the computational domain at the $(n+1)$th time level satisfy the governing equations (2.24) and (2.25). The discretized finite difference equations can be written in the following form:

$$(\bar{\phi}_t)_{i,j}^{n+1} + F_h(\bar{\phi}_x)_{i,j}^{n+1} - \frac{\mu^2 F_h}{3}(\bar{\phi}_{xxx})_{i,j}^{n+1} = -\zeta_{i,j}^{n+1} + \frac{\mu^2 F_h}{3}(\bar{\phi}_{xyy})_{i,j}^{n+1} - \frac{\epsilon}{2}(\bar{\phi}_x^2 + \bar{\phi}_y^2)_{i,j}^{n+1} - p_{i,j}, \tag{3.1}$$

$$(\zeta_t)_{i,j}^{n+1} + F_h(\zeta_x)_{i,j}^{n+1} = -(\bar{\phi}_{xx} + \bar{\phi}_{yy})_{i,j}^{n+1} + \epsilon F_h(2\bar{\phi}_x\bar{\phi}_{xx} + \bar{\phi}_x\bar{\phi}_{yy} + \bar{\phi}_y\bar{\phi}_{xy})_{i,j}^{n+1}. \tag{3.2}$$

The adopted finite difference scheme (3.1), (3.2) is of fully implicit type and is unconditionally stable. Note that the $O(\epsilon)$ forcing term in (2.25) has been omitted.

The three-time-level scheme is used to approximate the time derivative:

$$(\bar{\phi}_t)_{i,j}^{n+1} = \frac{3\bar{\phi}_{i,j}^{n+1} - 4\bar{\phi}_{i,j}^{n} + \bar{\phi}_{i,j}^{n-1}}{2\Delta t},$$
$$(\zeta_t)_{i,j}^{n+1} = \frac{3\zeta_{i,j}^{n+1} - 4\zeta_{i,j}^{n} + \zeta_{i,j}^{n-1}}{2\Delta t}.$$

A centred scheme is applied to approximate all spatial derivatives at the inner nodes of the computational mesh. The solution of the nonlinear equations (3.1) and (3.2) can be obtained iteratively. The initial value of the variables at the next time step is taken as the value at the nth step,

$$\bar{\phi}_{i,j}^{n+1,0} = \bar{\phi}_{i,j}^{n}, \quad \zeta_{i,j}^{n+1,0} = \zeta_{i,j}^{n},$$

in which the second superscript indicates the index of iteration. At each iterative step, the linear terms with the x-derivative are approximated implicitly on the left-hand side of equations and all other terms with nonlinearity and cross-derivatives are put on the right-hand side as the known for the next iteration. The iteration is done line by line on the nodes with the same transverse superscript j, from the symmetric plane ($j = 0$) to the truncated outer boundary ($j = jmax$). All variables take the latest value from the iteration. A sub-relaxation scheme is used to update the variables after each iteration.

At each iterative step k,

$$\frac{3\tilde{\zeta}_{i,j}^{n+1,k} - 4\zeta_{i,j}^{n} + \zeta_{i,j}^{n-1}}{2\Delta t} + F_h \frac{\tilde{\zeta}_{i+1,j}^{n+1,k} - \tilde{\zeta}_{i-1,j}^{n+1,k}}{2\Delta x}$$
$$= -(\bar{\phi}_{xx} + \bar{\phi}_{yy})_{i,j}^{n+1,k'} + \epsilon F_h (2\bar{\phi}_x\bar{\phi}_{xx} + \bar{\phi}_x\bar{\phi}_{yy} + \bar{\phi}_y\bar{\phi}_{xy})_{i,j}^{n+1,k'} \quad (3.3)$$

$$\frac{3\tilde{\bar{\phi}}_{i,j}^{n+1,k} - 4\bar{\phi}_{i,j}^{n} + \bar{\phi}_{i,j}^{n-1}}{2\Delta t} + F_h \frac{\tilde{\bar{\phi}}_{i+1,j}^{n+1,k} - \tilde{\bar{\phi}}_{i-1,j}^{n+1,k}}{2\Delta x} - \frac{\mu^2 F_h}{3} \frac{\tilde{\bar{\phi}}_{i+2,j}^{n+1,k} - 2\tilde{\bar{\phi}}_{i+1,j}^{n+1,k} + 2\tilde{\bar{\phi}}_{i-1,j}^{n+1,k} - \tilde{\bar{\phi}}_{i-2,j}^{n+1,k}}{2\Delta x^3}$$
$$= -\tilde{\zeta}_{i,j}^{n+1,k} + \frac{\mu^2 F_h}{3}(\bar{\phi}_{xyy})_{i,j}^{n+1,k'} - \frac{\epsilon}{2}(\bar{\phi}_x^2 + \bar{\phi}_y^2)_{i,j}^{n+1,k'} - p_{i,j}, \quad (3.4)$$

in which $\tilde{\zeta}_{i,j}^{n+1,k}$ and $\tilde{\bar{\phi}}_{i,j}^{n+1,k}$ are the prediction values of the $\zeta_{i,j}$ and $\bar{\phi}_{i,j}$ after the kth iteration. The superscript k' is used in the terms of the right-hand side since both the values at the $(k-1)$th and kth iterations are used to evaluate the derivatives.

The x-derivatives on the right-hand sides of (3.3) and (3.4) are obtained from the kth iterative value

$$(\bar{\phi}_x)_{i,j}^{n+1,k'} = \frac{\bar{\phi}_{i+1}^{n+1,k} - \bar{\phi}_{i-1}^{n+1,k}}{2\Delta x}, \quad (\bar{\phi}_{xx})_{i,j}^{n+1,k'} = \frac{\bar{\phi}_{i+1,j}^{n+1,k} - 2\bar{\phi}_{i,j}^{n+1,k} + \bar{\phi}_{i-1,j}^{n+1,k}}{\Delta x^2}.$$

The transverse derivatives are evaluated from

$$(f_y)_{i,j}^{n+1,k'} = \frac{f_{i,j+1}^{n+1,k-1} - f_{i,j-1}^{n+1,k}}{2\Delta y}, \quad (f_{yy})_{i,j}^{n+1,k'} = \frac{f_{i,j+1}^{n+1,k-1} - 2f_{i,j}^{n+1,k-1} + f_{i,j-1}^{n+1,k}}{\Delta y^2},$$

in which f denotes the velocity potential $\bar{\phi}$ or its first x-derivative $\bar{\phi}_x$.

The kth iterative values of $\bar{\phi}$ and ζ are obtained from

$$\bar{\phi}_{i,j}^{n+1,k} = \bar{\phi}_{i,j}^{n} + \omega_\phi(\tilde{\bar{\phi}}_{i,j}^{n+1,k} - \bar{\phi}_{i,j}^{n}), \quad \zeta_{i,j}^{n+1,k} = \zeta_{i,j}^{n} + \omega_\zeta(\tilde{\zeta}_{i,j}^{n+1,k} - \zeta_{i,j}^{n}),$$

in which ω_ϕ and ω_ζ are the relaxative factors for $\bar{\phi}$ and ζ respectively. The relaxation factor is related to the eigenvalue of the set of linear equations. A rigorous analysis of the eigenvalue of the discretized set of linear equations is almost impossible because of the complexity of the system. According to numerical experience, the under-relaxative factors ω_ϕ and ω_ζ take values in the range of (0.2, 1.0), and are functions of the spatial grid size and time step. Fine computational grids and a small time step need smaller relaxative factors than a numerical test with coarser grids. From the numerical tests, it is found that there exist critical relaxative factors, beyond which the iteration cannot converge and below which the number of iterations needed to reach convergence increases as the relaxative factors decrease. These optimal relaxative factors $\omega_{\phi,opt}$ and $\omega_{\zeta,opt}$ can be obtained by running the computer code for a few time steps and one can select the best values for the simulation of the free-surface flow for long time.

The implicit scheme is unconditionally stable, and its temporal and spatial accuracy is second order, i.e. $O(\Delta t^2)$, $O(\Delta x^2, \Delta y^2)$.

3.2. *Open boundary conditions*

The no-disturbance boundary conditions upstream are set as

$$\bar{\phi} = 0, \quad \zeta = 0 \quad \text{as} \quad x \to -\infty.$$

The computation will stop before the upstream-going waves hit the boundary.

The speed of the wave propagation downstream is much higher than that of the wave propagating upstream. Thus it is not appropriate to extend the downstream domain far enough downstream to satisfy the no-disturbance boundary condition. Suitable open boundary conditions are needed to act on the truncated boundaries and make the wave propagate outward with minimum reflection. It was shown that the reflective effect of sidewalls is the origin of the two-dimensional straight-crest upstream solitons in the channels of finite depth (see Katsis & Akylas 1987; Pedersen 1988). Therefore, the open boundary condition is crucial in order to capture the phenomenon of three-dimensional upstream solitons in open water. A Sommerfeld-type radiation condition is imposed on both the downstream boundary and transverse truncated boundary:

$$\frac{\partial \bar{\phi}}{\partial t} + C_\phi \frac{\partial \bar{\phi}}{\partial x} = 0, \quad \frac{\partial \zeta}{\partial t} + C_\zeta \frac{\partial \zeta}{\partial y} = 0,$$

in which C_ϕ, C_ζ are the phase velocities of the velocity potential and free-surface elevation respectively, which can be computed with Orlanski's scheme (Orlanski 1976); $\boldsymbol{n}$ is the normal unit vector on the truncated boundaries.

3.3. *Data smoothing*

With the progress of the calculation, error accumulation is unavoidable in the computational domain. The noise consists of waves with short wavelength and its amplification will grow and eventually contaminate the computational domain. A spatial filter is applied to smooth the free-surface profile (see Longuet-Higgins & Cokelet 1976; Nakos, Kring & Sclavounos 1993) each 40–100 time steps. Both five-point and seven-point schemes are tested and they generate almost same solution of $\bar{\phi}$ and ζ. In this paper, the five-point smoothing scheme was used.

4. Numerical results and discussion

The mathematical model and numerical schemes described in § 2 and § 3 are applied to simulate the nonlinear long waves induced by a pressure distribution and a thin ship travelling near the critical speed in shallow water. In the three-dimensional case, the wavenumber k and wave amplitude a are difficult to define uniquely, though this causes no problems in the derivation of the governing equations and the design of numerical schemes. In the following numerical computation, the water depth h is chosen to scale all the spatial variables and the time scale becomes $\sqrt{h/g}$.

4.1. *Nonlinear waves generated by a pressure distribution*

We consider the case of nonlinear long waves generated by a pressure distribution of sinusoidal shape moving on the free surface. The pressure acts inside a rectangle symmetric about the x- and y-axes with length L and width B and vanishes outside the rectangle. The pressure distribution is defined as

$$p(x, y) = \overline{P} \cos^2\left(\frac{\pi x}{L}\right) \cos^2\left(\frac{\pi y}{B}\right), \quad -\frac{L}{2} < x < \frac{L}{2}, \quad -\frac{B}{2} < y < \frac{B}{2},$$

in which $\overline{P}$ is the peak value of the pressure distribution. Due to symmetry, the computation is only carried out in the positive half of the fluid domain with $y \geqslant 0$. The computational mesh is orthogonal and the longitudinal and transverse grid sizes are $\Delta x = \Delta y = 0.25$, respectively. The time step is $\Delta t = 0.2$. We choose the non-dimensional size of the pressure rectangle as $L = 10.0$ and $B = 4.0$. The pressure is assumed to be forced impulsively at the initial time when the velocity and free-surface elevation are both zero. The computational domain is $x_{upstream} = -60.0$, $x_{downstream} = 100.0$ and the transverse boundary is truncated at $y_{span} = 240.0$. Oranski open boundary conditions are applied on the downstream boundary and the transverse boundary so that the outgoing wave propagates outside the computational domain with very little reflection. In addition to the standard resolution $\Delta x = \Delta y = 0.25$ and $\Delta t = 0.2$, computations have also been made for $\Delta x, \Delta y = 0.10, 0.25, 0.40$, $\Delta t = 0.05, 0.1, 0.2$. It is found that the wave elevation, especially of the upstream nonlinear long waves, converges for the grid sizes 0.25 and time step 0.2. In fact, the values of grid size and time step would become much smaller if we employed the wavelength of upstream waves as the spatial scale; unfortunately it cannot be determined *a priori*.

Figure 1 presents perspective views of the wave patterns generated by a pressure distribution travelling at a critical speed with magnitude $\overline{P} = 0.30$ at different stages of the development of the waves. There is no reflection from the side boundary and the crestlines of the upstream waves are always curved, with the curvature decreasing as the wave moves forward. At $t = 1200$, four upstream solitary waves have been radiated from the disturbance and a new one is developing. The wave peak occurs ahead of the front edge of the pressure distribution and a nearly steady wave hump originates there and extends downstream obliquely, behaving like a barrier between the upstream solitary wave region and the downstream divergent wave region. The wave reaches its minimum beneath the pressure distribution. Both transverse and divergent wave systems develop behind the disturbance and the interaction between these two wave systems is clear. The transverse wave packet has a mean downstream group velocity and a depressed water surface, analogous to that in the two-dimensional case, forms behind the trailing edge of the pressure patch (see Mei 1986).

Figure 2 shows the wave profiles on the symmetry plane $y = 0$ induced by pressure distributions with different magnitudes $\overline{P} = 0.20, 0.30, 0.40, 0.50$. It is clear that a succession of solitary waves radiate upstream, the wave amplitude decreasing as it

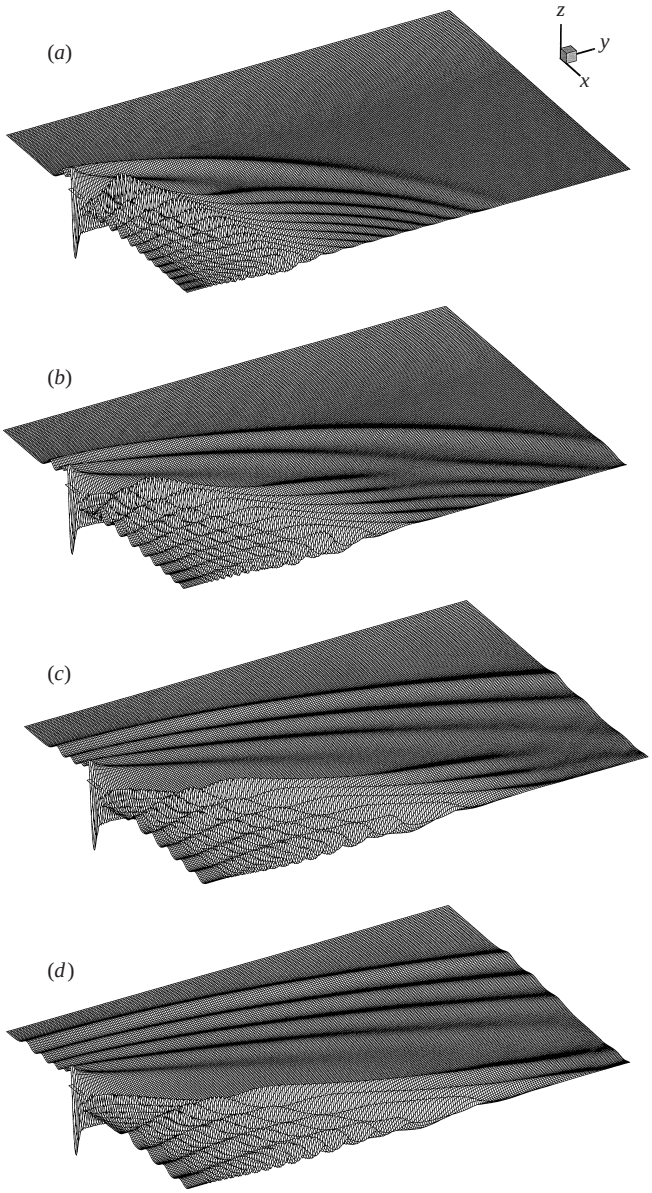

FIGURE 1. Wave evolution generated by a pressure distribution in an unbounded domain. $F_h = 1.0$, $\overline{P} = 0.30$: (*a*) $t = 200$; (*b*) $t = 400$; (*c*) $t = 800$; (*d*) $t = 1200$.

moves forward. The mean level behind the pressure distribution is lower than the still free surface and connects to a transverse wave train propagating downstream. There exists significant interaction, including the transfer of mass, momentum and energy, between neighbouring solitons. This can be proved by the study of free soliton, see below, which shows a different type of wave development without forcing. The magnitude of the pressure plays an important role in the wave amplitude, phase velocity and the period of soliton generation. With a higher forcing pressure, the wave amplitudes and velocities of both upstream and downstream waves increase.

We define the maximum value of the three-dimensional solitary wave on the symmetry plane as its amplitude and show the correlation between the wave amplitude

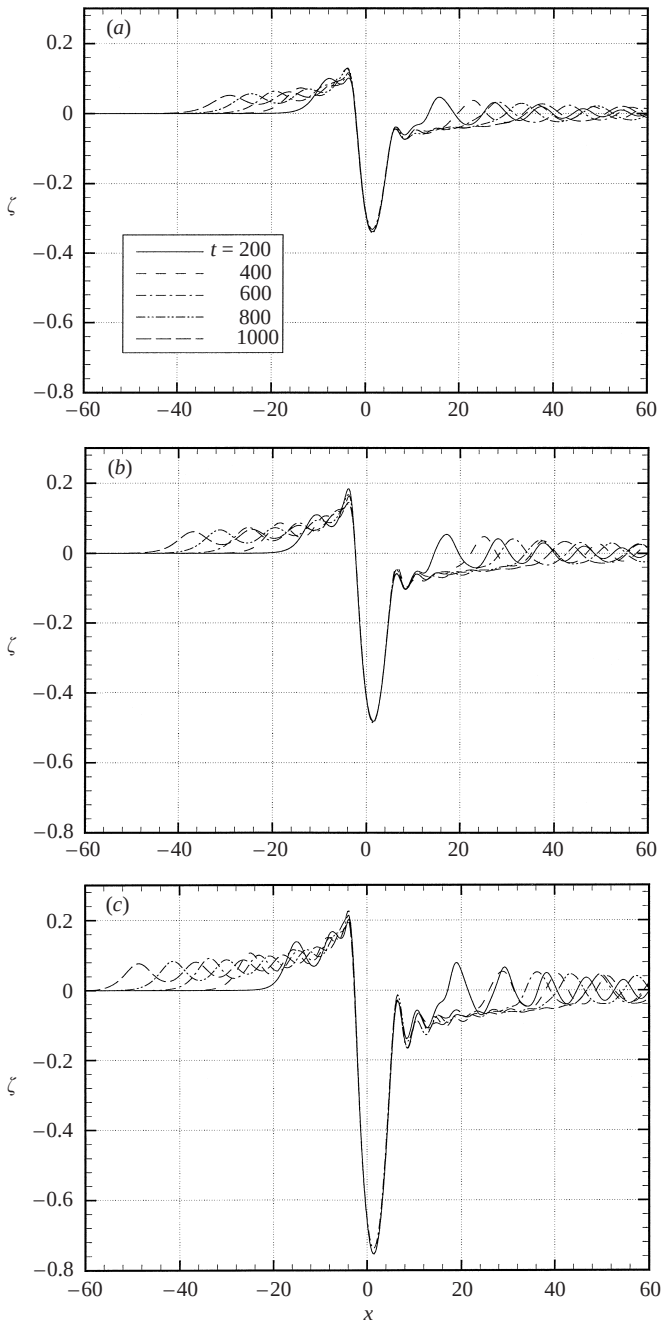

FIGURE 2. Wave profile at $y = 0$ generated by a pressure distribution, $F_h = 1.0$: (*a*) $\overline{P} = 0.20$; (*b*) $\overline{P} = 0.30$; (*c*) $\overline{P} = 0.50$.

and crest position in figure 3. For different pressures, the relation between the soliton crest position x_c and the product of its amplitude and time $A_c t$ is linear and can be approximated by the formula

$$x_c + \tfrac{2}{3}A_c t = C(\overline{P}) \tag{4.1}$$

in which $C(\overline{P})$ is a constant varying with the pressure distribution.

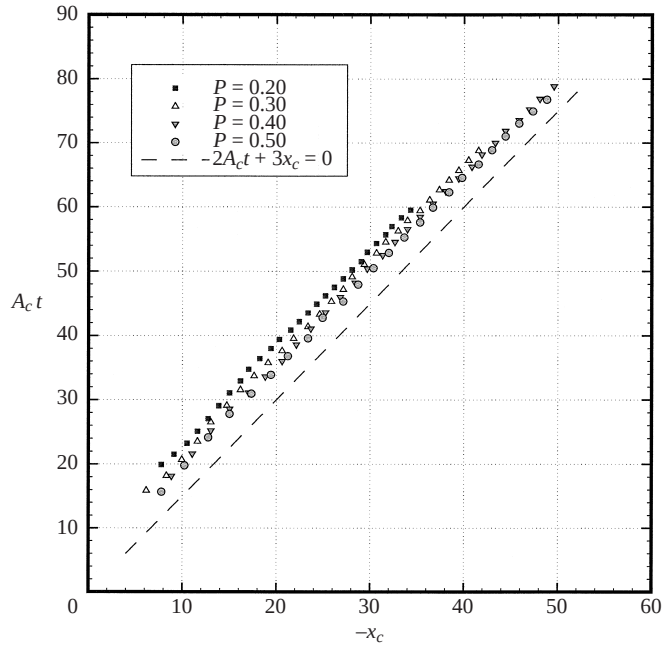

FIGURE 3. x_c vs. $A_c t$ for the leading soliton generated by a pressure distribution, $F_h = 1.0$.

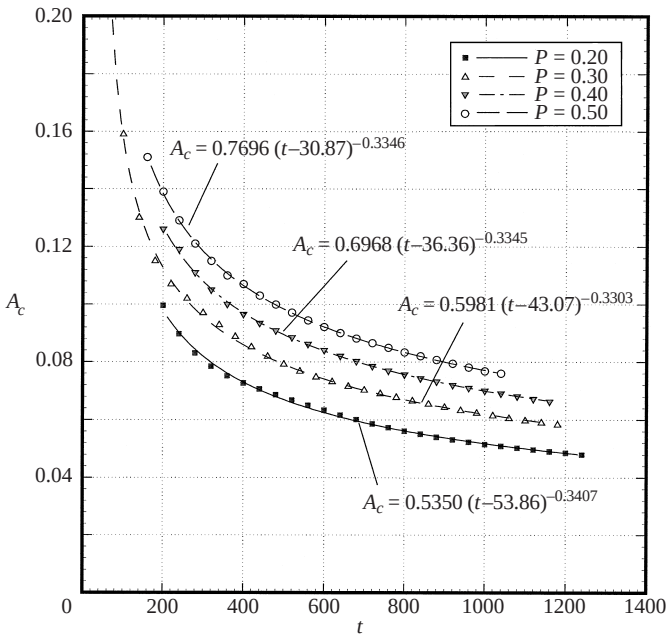

FIGURE 4. Wave amplitude A_c of the leading soliton at different times, $F_h = 1.0$. The lines are fitting curves.

The amplitudes of the leading solitons at different times are drawn in figure 4 and are approximated by the formula

$$A_c(t) = A_1(t - t_0)^{\gamma} \tag{4.2}$$

in which A_1 and t_0 are constants related to the initial wave amplitude and the escape

$\overline{P}$	A_1	t_0	γ
0.20	0.5350	53.86	−0.3407
0.30	0.5981	43.07	−0.3303
0.40	0.6968	36.36	−0.3345
0.50	0.7696	30.87	−0.3346

TABLE 1. Approximation for the wave amplitude of the leading soliton generated by a pressure distribution, $F_h = 1.0$.

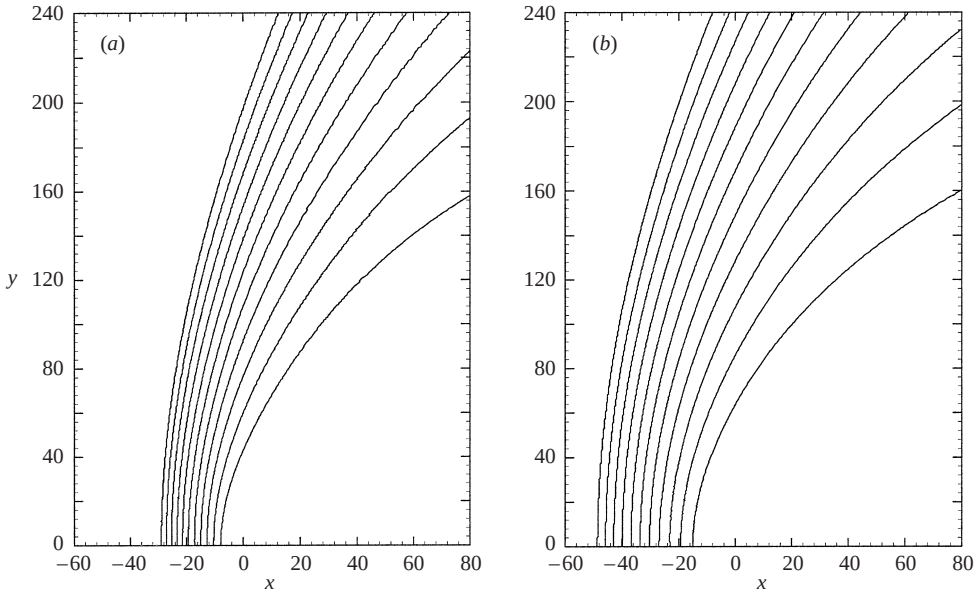

FIGURE 5. Crestline of the leading soliton generated by a pressure distribution from $t = 200$ to $t = 1000$ with interval 80. $F_h = 1.0$: (*a*) $\overline{P} = 0.20$; (*b*) $\overline{P} = 0.50$.

time of the soliton from the pressure disturbance; γ is the decay rate of the leading soliton. Table 1 shows the result of the approximation and shows that the wave amplitude of the leading soliton decays asymptotically at a rate of $O(t^{-1/3})$ for large t.

Figure 5 shows the evolution of the crestline of the leading soliton generated by pressure distributions of different magnitudes. The first crestline is recorded at $t = 200$, in which the soliton has detached from the forcing, and the time interval between the crestlines is $\Delta t = 80$. As shown, the curvature of the isophasal crestline decreases as the soliton moves ahead. The crestlines are drawn on a log-log scale in figure 6(*a*). Surprisingly, a straight line is predicted with almost the same slope at different times. The crestline of the leading soliton is approximated by the formula

$$y = \alpha_1(t)(x - x_c)^{\beta(t)}. \tag{4.3}$$

The approximation indices $\beta(t)$ at different times are plotted in figure 6(*b*); $\beta(t)$ takes a mean value close to 0.5 and varies very slowly with respect to time, independently of the forcing pressure magnitude and the wave amplitude. This shows that the crestline is nearly a parabola that can be approximated by

$$y^2 = \alpha(t)(x - x_c) \tag{4.4}$$

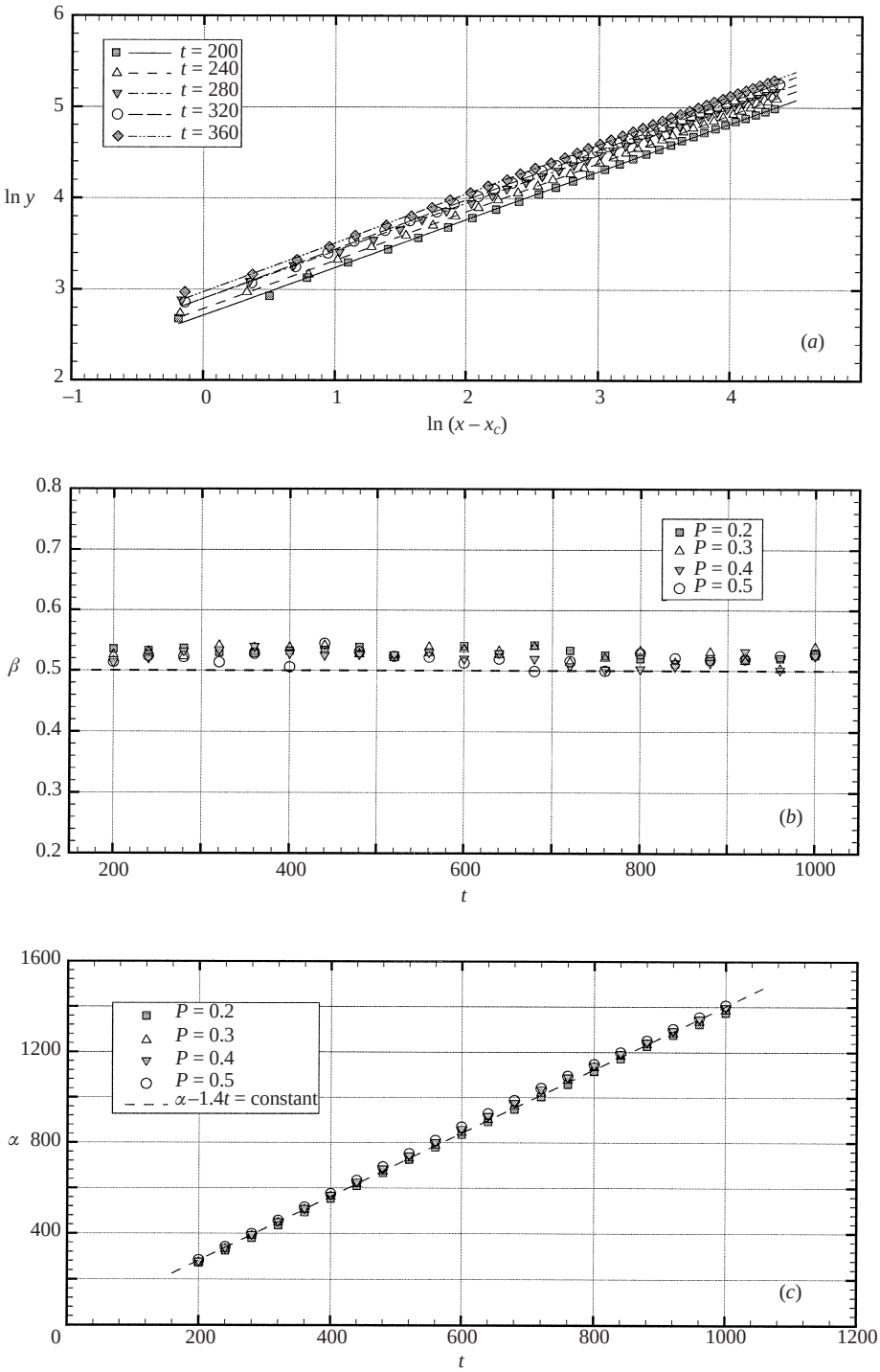

FIGURE 6. Geometry properties of the crestline of the leading soliton, $F_h = 1.0$: (*a*) log-log scale plot of crestline for $\overline{P} = 0.30$; (*b*) index $\beta(t)$; (*c*) latus rectum $\alpha(t)$. The lines in (*a*) are fitting curves.

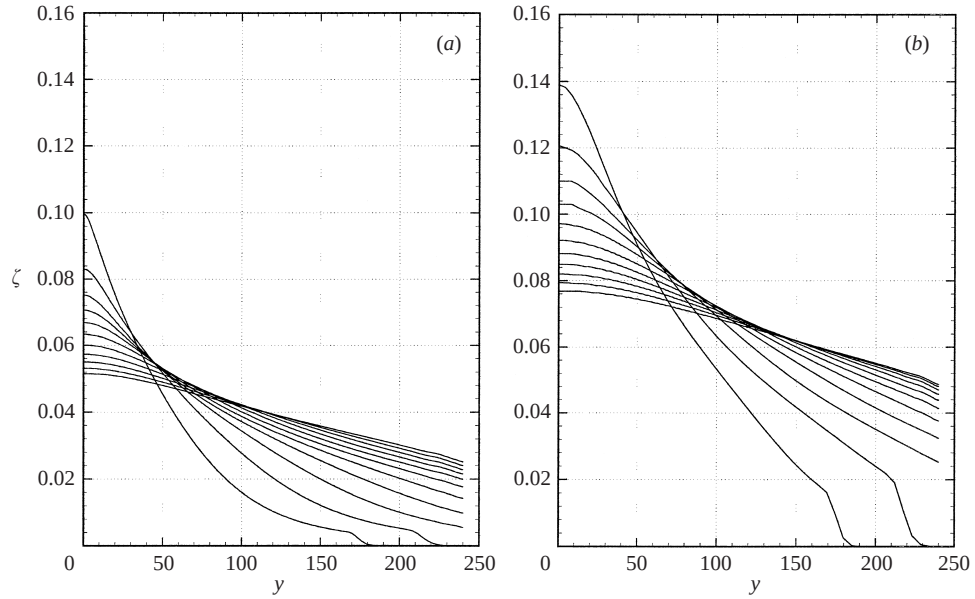

FIGURE 7. Wave amplitude along the crestline of the leading soliton generated by a pressure distribution from $t = 200$ to $t = 1000$ with interval 80. $F_h = 1.0$: (*a*) $\overline{P} = 0.20$; (*b*) $\overline{P} = 0.50$.

in which $\alpha(t)$ is the length of the *latus rectum* (the chord perpendicular to the symmetry axis which passes through the focus of a parabola). Its dependence on time is shown in figure 6(*c*) and a linear correlation is found. The slope of $\alpha(t)$ is about 1.40 and independent of the magnitude of the forcing pressure.

Based on the analysis shown above, we can see that, when time is large enough, the crestline of the leading soliton forced in open sea takes the asymptotic form

$$x + A_0 t^{2/3} = B_0 \frac{y^2}{t} \tag{4.5}$$

in which A_0 and B_0 are constants determined by the initial value of the waves.

The wave amplitude along the crestline of the leading wave is shown in figure 7 with the time interval $\Delta t = 80$. The wave is steeper at its wave front in the y-direction, which is a consequence of the impulsive start of the forcing pressure. As time goes on, the wave spreads in the lateral direction. The slope of the crestline decreases slowly when the soliton moves forward.

The three-dimensional upstream solitary waves can also be generated in the subcritical and supercritical cases. Figure 8(*a*, *c*) shows the perspective and contour plots of the wave patterns at $F_h = 0.9$ and 1.1. The wave profiles on the symmetry plane are drawn in figure 9. At $F_h = 0.9$, the leading soliton is followed by a succession of solitons with decreasing wave amplitude. The positive peak of the wave is reached at the trailing edge of the pressure patch and the downstream wake is much more significant than the upstream waves. The wave amplitude and phase velocity of the solitons increase as the Froude number increases, whereas the amplitude of the downstream waves decreases. As shown in figure 9, there is no depressed water behind the disturbance at $F_h = 0.9$. However, the mean water level of the central line of the downstream region is below $z = 0$ at $F_h = 1.1$. A very interesting property which exists exclusively in three dimensions is that the upstream soliton is blocked for the supercritical case. The phase velocity of the

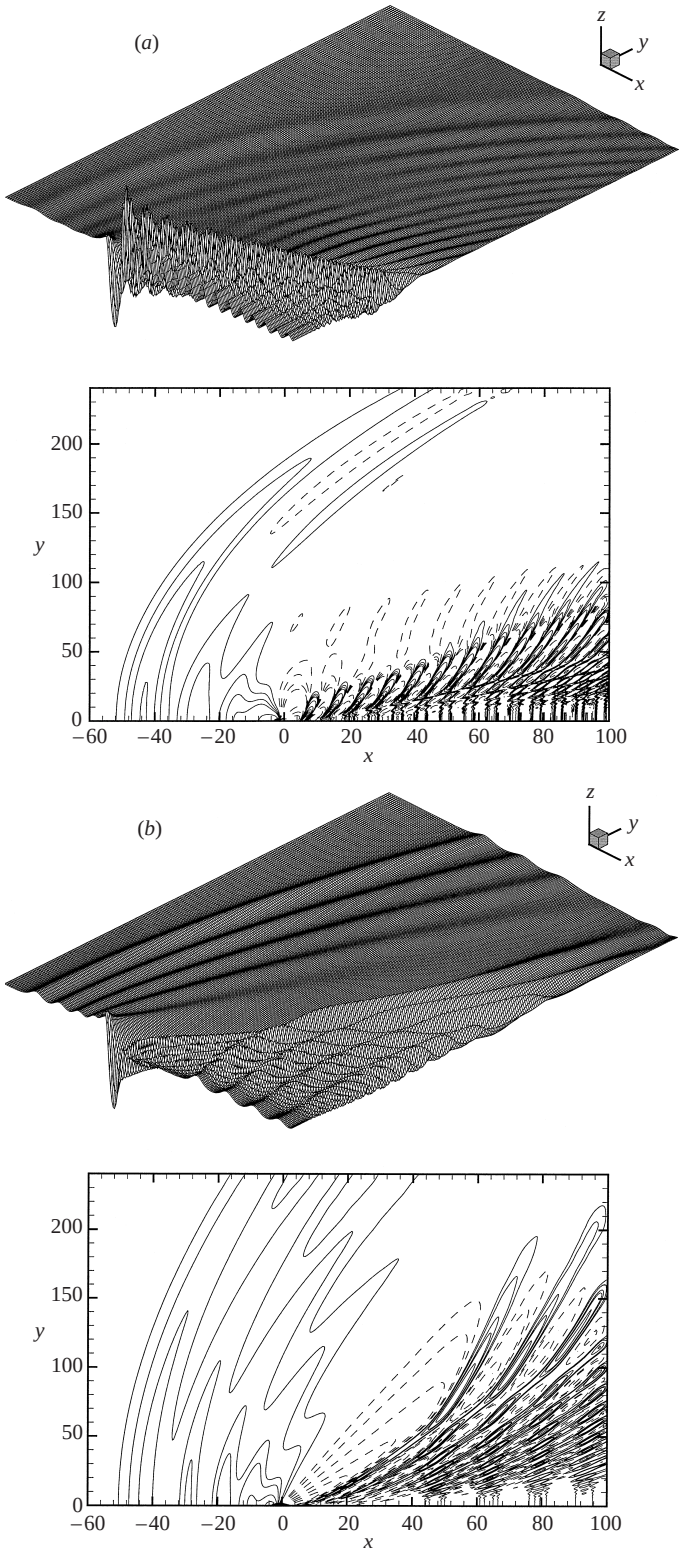

FIGURE 8(*a*, *b*). For caption see facing page.

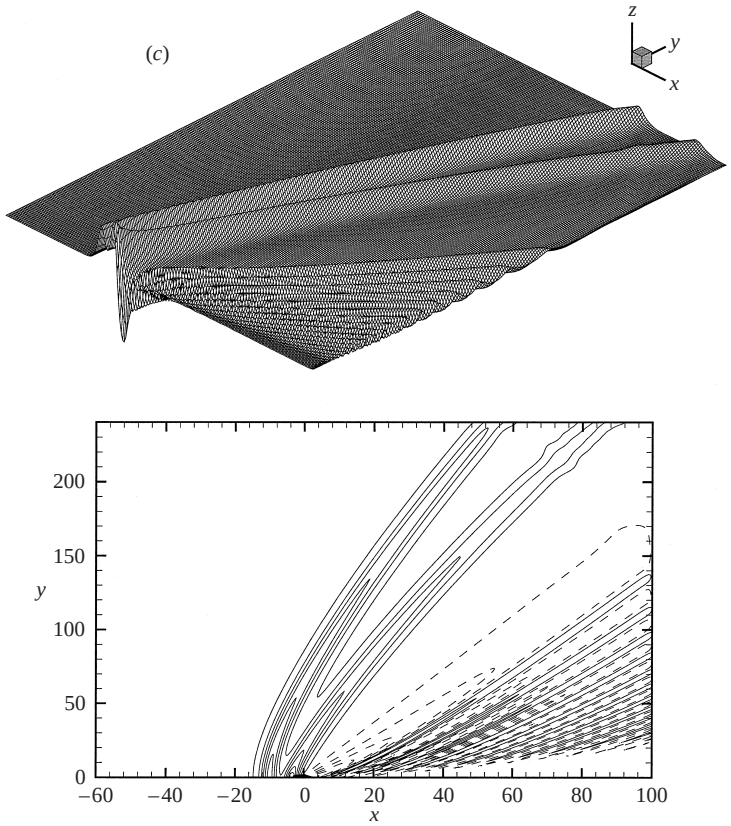

FIGURE 8. Wave patterns and contours at transcritical speeds. $\overline{P} = 0.30$: (*a*) $F_h = 0.9$, $t = 400$; (*b*) $F_h = 1.0$, $t = 1200$; (*c*) $F_h = 1.1$, $t = 1200$.

leading soliton tends to that of the disturbance F_h as its amplitude decreases to a critical value, which is 0.23 seen in figure 9(*b*). The leading soliton shifts a little from $t = 1600$ to $t = 2000$ with almost no change of the amplitude. During this time, the curvature of the leading soliton decreases slowly to form a more straight crestline.

The free propagation of three-dimensional nonlinear long waves is also investigated. Instead of letting a steady pressure act on the free surface for all time $t > 0$, we turn off the pressure distribution at some time, in this case at $t = 200$, when the first crest has been generated and the second has not yet escaped from the source. The free-surface elevation and velocity at $t = 200$ become the initial value for the nonlinear wave evolution without forcing.

Figure 10 shows the wave profile on the symmetry plane without forcing by the finite-time action of the pressure of magnitude $\overline{P} = 0.40$ and 0.60. The large free-surface elevation around the pressure distribution is smoothed rapidly. The leading soliton detaches from the second soliton and the mean water level between two successive waves becomes zero. The wave amplitude of the second soliton is smaller than the leading one. The interaction between the leading soliton and its successor is negligible and it can be considered as a free soliton in three dimensions.

The relation between the crest displacement x_c and the product $A_c t$ is shown in

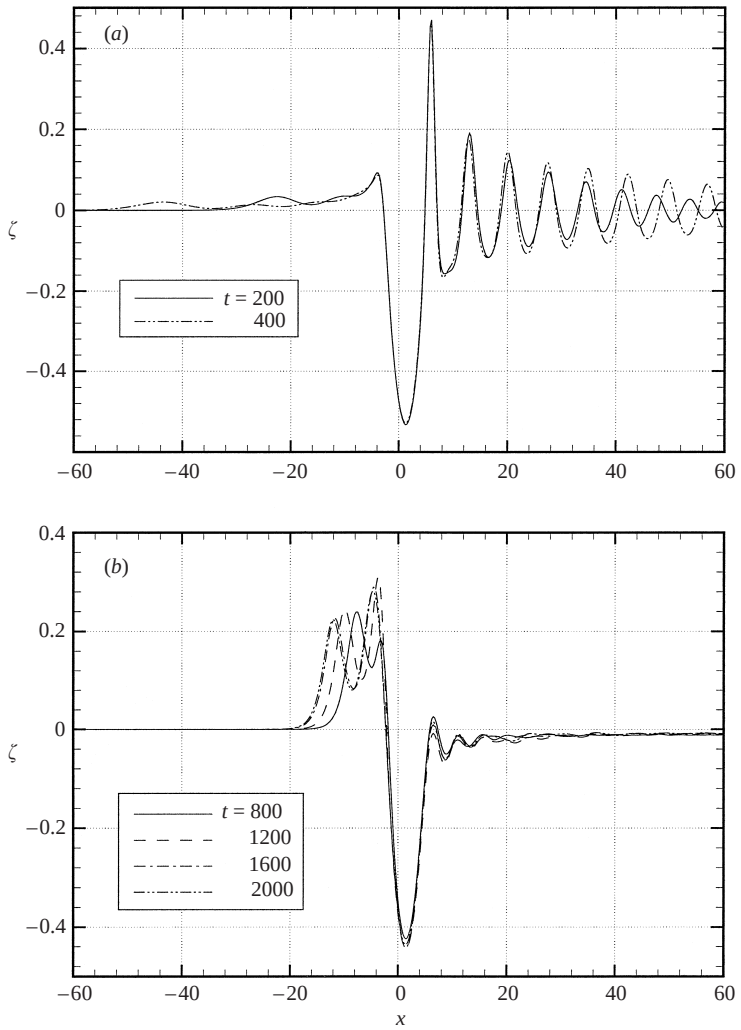

FIGURE 9. Wave profile at $y = 0$ generated by a pressure distribution, $\overline{P} = 0.30$: (*a*) $F_h = 0.9$; (*b*) $F_h = 1.1$.

figure 11. The slope of $A_c t$ as a function of $-x_c$ decreases from 3/2, which is illustrated in figure 3, to nearly 1/3. The slope of the free soliton is independent of the initial values which are different for the wave pattern generated by a pressure with different magnitude.

The wave amplitude of the leading free soliton at different times is displayed in figure 12 for $\overline{P} = 0.30, 0.40, 0.50, 0.60$. The regressive results for the variables in (4.2) are listed in table 2. The decay rate of the free soliton amplitude with respect to time is about -0.785.

The decay rate of a free three-dimensional soliton is larger than a forced one which interacts with the next soliton. In two dimensions, a free soliton can keep its shape and propagate permanently. By the conservation of energy, Lee & Grimshaw (1990) deduced that the amplitude of a free propagating soliton decays at a rate of $O(t^{-2/3})$ by assuming that the amplitude along the isophasal crestline is constant. From the computation, we found that the wave amplitude of the leading soliton

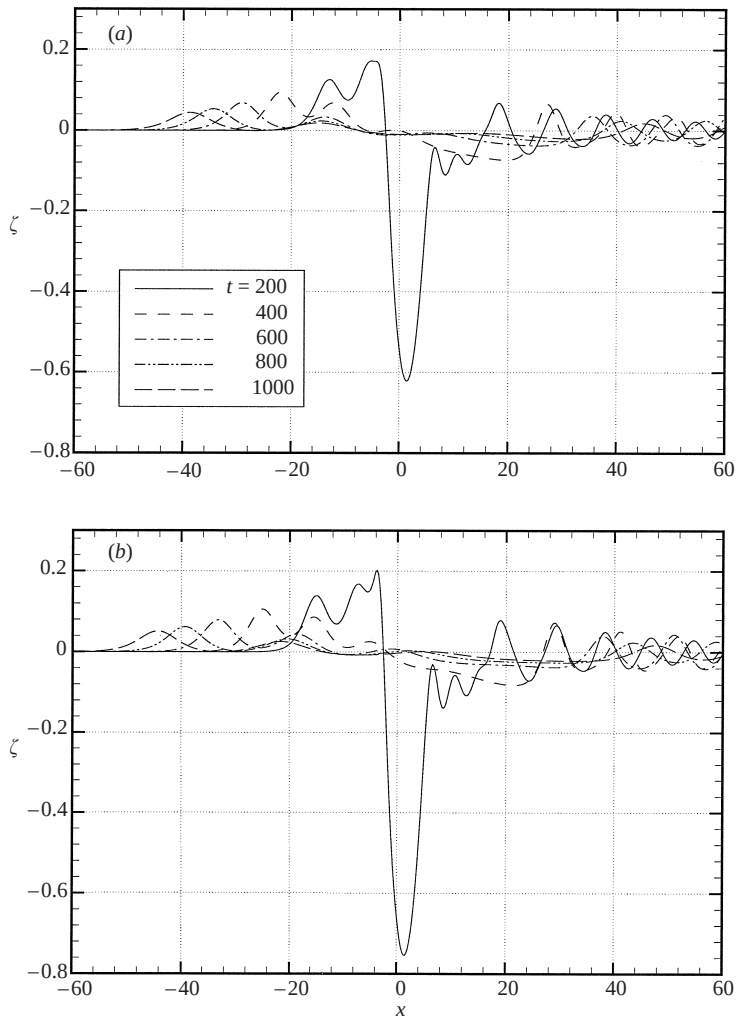

FIGURE 10. Wave profile at $y = 0$ of a free three-dimensional soliton, $F_h = 1.0$: (*a*) $\overline{P} = 0.30$; (*b*) $\overline{P} = 0.60$.

$\overline{P}$	A_1	t_0	γ
0.30	7.79	85.06	−0.7850
0.40	9.65	62.17	−0.7863
0.50	11.16	57.91	−0.7861
0.60	12.36	38.20	−0.7830

TABLE 2. Approximation for the wave amplitude of the free leading soliton, $F_h = 1.0$.

spreads laterally. It is found that the crestline of the leading free soliton is still nearly a parabola by fitting the crestline by (4.3) and obtaining the index $\beta(t)$ close to 0.50. The *latus rectum* of its parabolic crestline is a linear function of time with steeper slope 1.60 compared with the solitons generated by a constant applied pressure forcing.

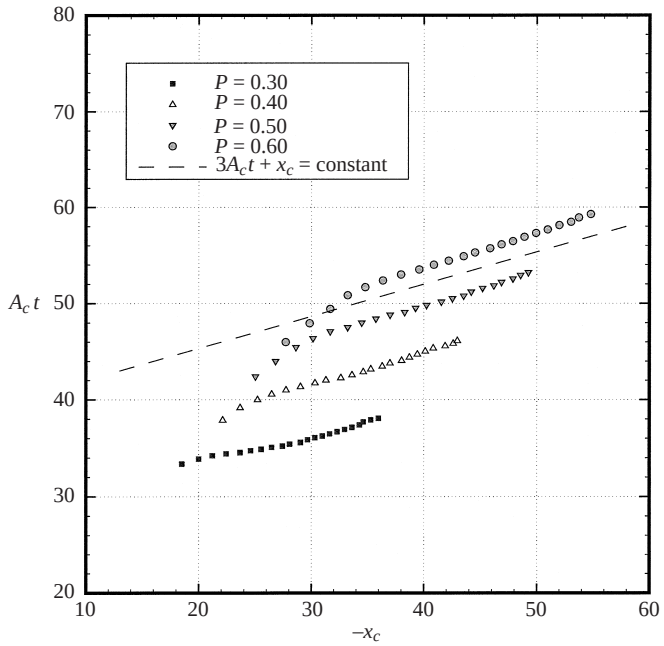

FIGURE 11. x_c vs. $A_c t$ of the free leading three-dimensional soliton, $F_h = 1.0$.

4.2. *Nonlinear waves generated by a thin ship*

For simplicity, we use a strut which extends to the sea bed and has the same width throughout the depth to simulate a high-speed vessel with more complicated hull shape. The shape of the water line is defined as

$$b(x) = \frac{B}{2}\cos^2\frac{\pi x}{L}, \quad -\frac{L}{2} \leqslant x \leqslant \frac{L}{2},$$

in which B and L are the beam width and length of the ship. An advantage of this choice is that there is no jump of the normal vector along the waterline near the bow and stern. We consider a strut of length $L = 10.16$. Different beam widths are used to vary the slenderness of the strut. The computational domain is chosen as

$$-80 < x < 100, \quad 0 < y < 240.$$

The grid size is taken as $\Delta x = 0.25$ and $\Delta y = 0.4$. The time step is $\Delta t = 0.15$.

Figure 13 shows the perspective views of the wave pattern at $t = 800$ generated by struts of slenderness $B/L = 0.05$, 0.10, 0.15, 0.20 travelling at the critical speed $F_h = 1.0$. As shown, three dimensional solitary waves radiate in front of the strut periodically. The amplitude of the three-dimensional soliton decays as it moves upstream. The wave amplitude and frequency of wave generation increase as the strut becomes less slender. Shorter waves are generated in the downstream area as B/L increases, though the geometry of the upstream solitons does not change much. A transverse wave system is formed in a wedge-like region behind the strut and a system of divergent wave trains is formed outside the wedge. The performance of the Oranski open boundary condition becomes a little worse when the incident wave height increases as the strut becomes fat. Small reflective waves can be seen to interact with the upstream solitons and generate small fluctuations along the crests.

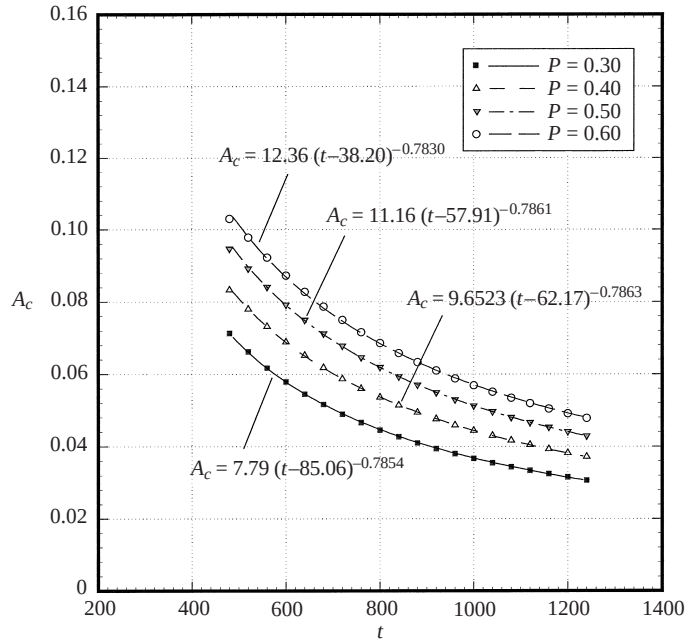

FIGURE 12. Wave amplitude A_c of the free leading three-dimensional soliton, $F_h = 1.0$. The lines are fitting curves.

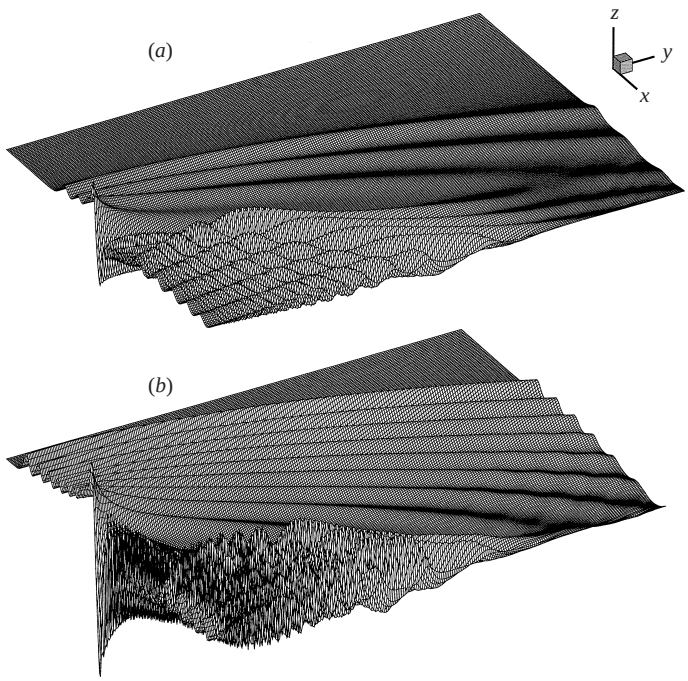

FIGURE 13. Wave pattern generated by a strut in open sea. $F_h = 1.0$, $t = 800$: (*a*) $B/L = 0.05$; (*b*) $B/L = 0.20$.

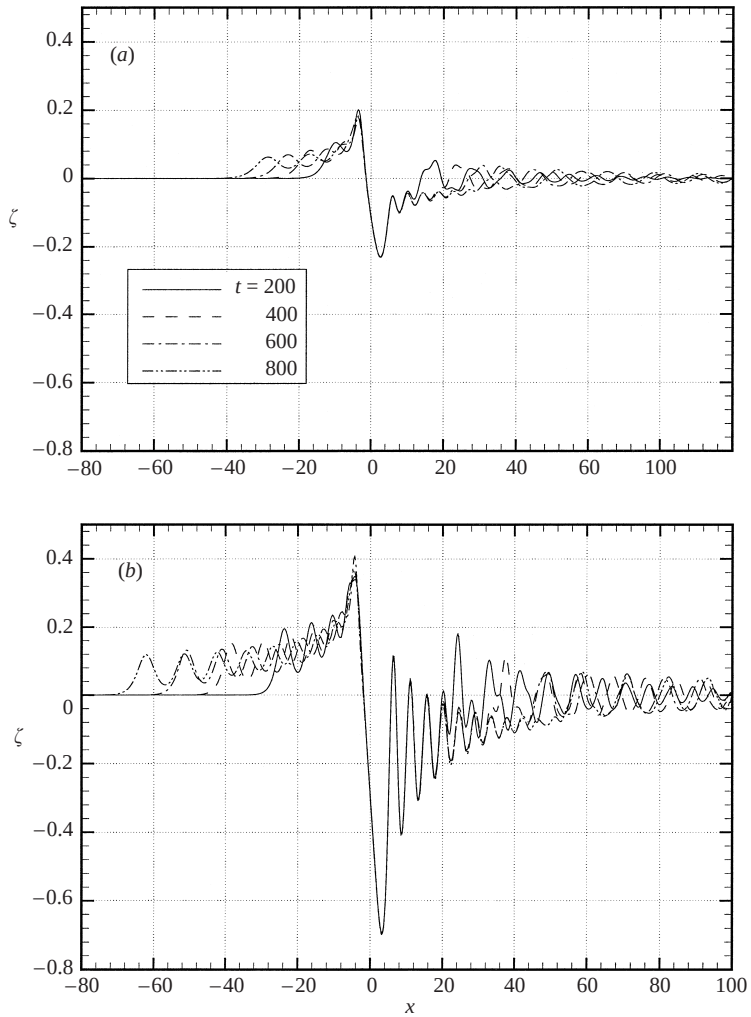

FIGURE 14. Wave profile at $y = 0$ generated by a strut, $F_h = 1.0$: (*a*) $B/L = 0.05$; (*b*) $B/L = 0.20$.

The free-surface elevations on the symmetry plane $y = 0$ generated by struts with different beam–length ratios travelling at a critical speed are drawn in figure 14. The peak value of the free-surface elevation occurs at about $x = -4.0$, a small distance behind the bow, a phenomenon observed in steady ship bow waves. The maximum negative wave elevation occurs near $x = 4.0$, a little ahead of the stern. The mean water level at $y = 0$ in the downstream region is below the still sea level and the depressed region elongates with time. As B/L increases, the downstream waves become pronounced and their wave heights increase. Comparing with figure 2, the downstream wave systems generated by a pressure distribution are more smooth than those by the strut. The ratio between the maximum negative wave elevation and the maximum positive wave elevation is smaller for the waves of the strut than those of the pressure distribution.

By fitting the leading wave amplitude with time by (4.2), we also find that the index γ is close to $-1/3$. The fitting results are listed in table 3 for struts with different beam–length ratios. The dependence of the phase velocity of the leading

B/L	A_1	t_0	γ
0.05	0.5900	41.10	−0.3379
0.10	0.7792	32.95	−0.3323
0.15	0.9659	27.28	−0.3356
0.20	1.1265	21.48	−0.3373

TABLE 3. Approximation for the wave amplitude of the leading soliton generated by a strut, $F_h = 1.0$.

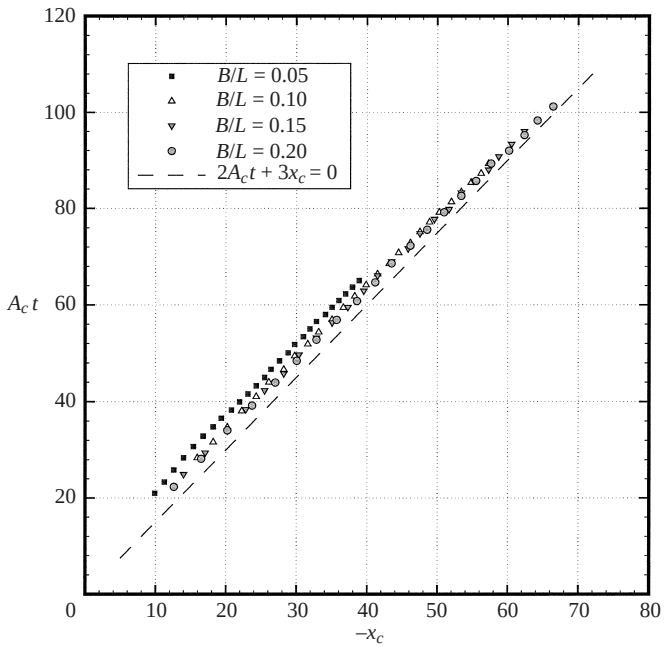

FIGURE 15. x_c vs. $A_c t$ of the leading soliton generated by a strut, $F_h = 1.0$.

soliton generated by the ship on its amplitude can be found from figure 15. A linear relation exists between x_c and $A_c t$ with a slope approximately of 3/2. The slope is independent of the slenderness of the strut. From table 3, the parameter t_0, which is the starting instant of soliton-like crest, is of $O(10)$. Compared with the time scale of the nonlinear wave evolution $t \sim O(10^3)$, t_0 is very small. Therefore, the phase velocity can be approximated as

$$V_c = -\frac{2}{3}\frac{\mathrm{d}}{\mathrm{d}t}(tA_c(t)) \approx -\tfrac{2}{3}(1+\gamma)A_c = \tfrac{4}{9}A_c,$$

which is applicable for the forced wave generated by a pressure distribution, source or underwater topography travelling at the critical speed.

Analysis of the geometry of the crestline of the leading soliton shows that the crestline is almost a perfect parabola whose curvature decreases with time. Using (4.4), we find that the slope of $\alpha(t)$ is about 1.40 and independent of the geometry of the strut.

Figure 16 shows the wave profile at the symmetry plane generated by a strut of $B/L = 0.10$ at speed $F_h = 0.9$ and 1.1. At subcritical speed $F_h = 0.9$, the precursor

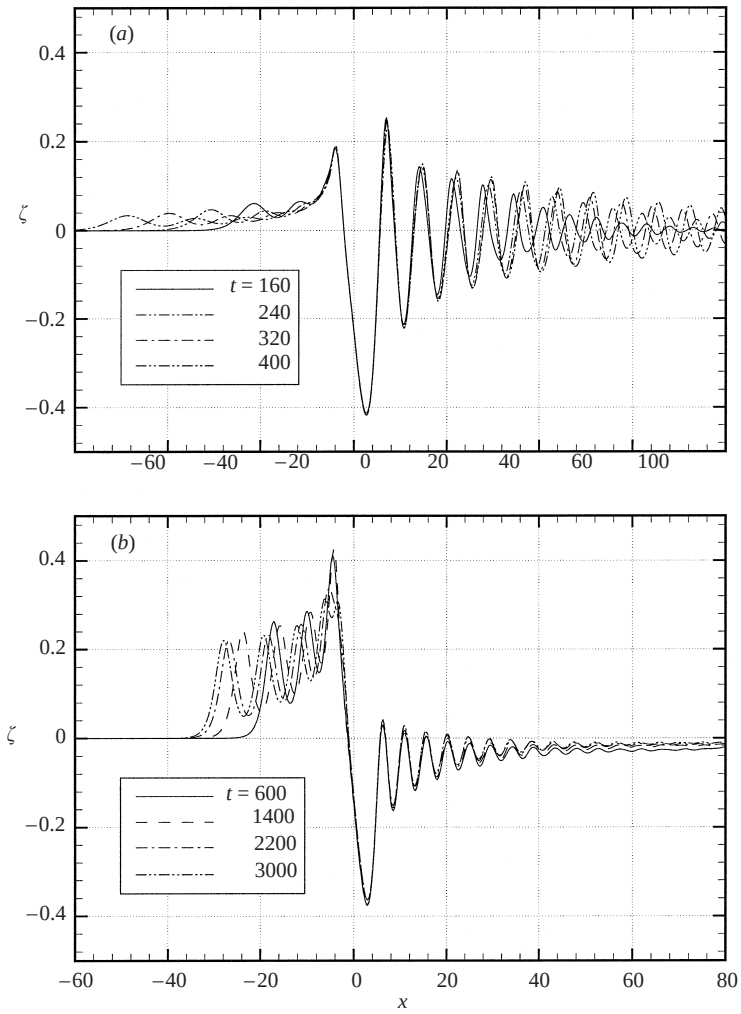

FIGURE 16. Wave profile at $y = 0$ generated by a strut, $B/L = 0.10$: (*a*) $F_h = 0.9$; (*b*) $F_h = 1.1$.

solitary wave decrease in amplitude as it moves upstream. At the supercritical speed $F_h = 1.1$, the leading soliton slows when its amplitude tends to 0.22, which is nearly $F_h^2 - 1$, the critical wave amplitude in a restricted channel for supercritical solitons. The leading soliton will eventually move at the same speed as the strut. The mean sea level of the downstream wave profile at $y = 0$ is below the still free surface. Both the upstream and downstream profile at the symmetry plane tends to be steady.

5. Conclusions

A modified generalized Boussinesq equation is derived to formulate the nonlinear long waves generated by a disturbance, which could be a pressure distribution, ship or underwater topography, travelling at transcritical speeds in shallow water in a restricted channel or open sea. The balance between nonlinearity and dispersive effects for the long wave causes the generation of solitary waves propagating upstream ahead of the disturbance. An effective implicit finite difference method is applied to

solve the nonlinear wave problem numerically. At each time step, an under-relaxation iterative procedure is used. A thin-ship approximation is used to study the solitons generated by a high-speed vessel in shallow water.

In the horizontally unbounded domain, three-dimensional solitary waves are generated ahead of the disturbance of a pressure distribution or an advancing ship. The crestline of the leading soliton is approximately a parabola with its *latus rectum* proportional to time, making the crestline curvature decrease as it moves forward. The decay rate of the wave amplitude is found to be $O(t^{-1/3})$ for the forced leading soliton and $O(t^{-0.78})$ for the free propagating three-dimensional solitary wave. Moreover, in the supercritical case the upstream soliton does not detach from the disturbance as is found to be the case in the critical and subcritical case. In the supercritical case, the steady state can be reached with several soliton parabolic humps formed in front of the disturbance and the wave amplitude of the leading soliton tends to $(F_h^2 - 1)h$.

REFERENCES

Akylas, T. 1984 On the excitation of long nonlinear water waves by a moving pressure distribution. *J. Fluid Mech.* **141**, 455–466.

Bai, K. J., Kim, J. W. & Kim, Y. H. 1989 Numerical computations for a nonlinear free surface flow problem. In *Proc. 5th Intl Conf. on Numer. Ship Hydrodyn., Hiroshima, Japan* (ed. K. Mori), pp. 403–418. National Academy Press.

Casciola, C. M. & Landrini, M. 1996 Nonlinear long waves generated by a moving pressure disturbance. *J. Fluid Mech.* **325**, 399–418.

Chen, X. N. & Sharma, S. D. 1995 A slender ship moving at a near-critical speed in a shallow channel. *J. Fluid Mech.* **291**, 263–285.

Choi, H. S., Bai, K. J., Kim, J. W. Kim & Cho, H. 1990 Nonlinear free surface waves due to a ship moving near the critical speed in a shallow water. In *Proc. 18th Symp. Naval Hydrodyn., Ann Arbor, Michigan*, pp. 173–190.

Choi, H. S. & Mei, C. C. 1989 Wave resistance and squat of a slender ship moving near the critical speed in restricted water. In *Proc. 5th Intl Conf. on Numer. Ship Hydrodyn., Hiroshima, Japan* (ed. K. Mori), pp. 439–454. National Academy Press.

Cole, S. J. 1985 Transient waves produced by flow past a bump. *Wave Motion* **7**, 579–587.

Ertekin, R. C., Webster W. C. & Wehausen J. V. 1984 Ship-generated solitons. In *Proc. 15th Symp. Naval Hydrodyn., Hamburg, Germany*, pp. 347–364.

Ertekin, R. C., Webster, W. C. & Wehausen, J. V. 1986 Waves caused by a moving disturbance in a shallow channel of finite width. *J. Fluid Mech.* **169**, 275–292.

Hamer, M. 1999 Solitary killers. *New Scientist* No. 2201, 163, pp. 18–19.

Huang, D. B., Sibul, O. J., Webster, W. C., Wehausen, J. V., Wu, D. M. & Wu, T. Y. 1982 Ships moving in the transcritical range. In *Proc. Conf. on Behavior of Ships in Restricted Waters, Varna, Bulgaria.*, vol. 2, pp. 26/1–10.

Katsis, C. & Akylas, T. R. 1987 On the excitation of long nonlinear water waves by a moving pressure distribution. Part 2. Three-dimensional effects. *J. Fluid Mech.* **177**, 49–65.

Lee, S. J. & Grimshaw, R. H. J. 1990 Upstream-advancing waves generated by three-dimensional moving disturbances. *Phys. Fluids* A **2**, 194–201.

Lee, S. J., Yates, G. T. & Wu, T. Y. 1989 Experiments and analyses of upstream-advancing solitary waves generated by moving disturbances. *J. Fluid Mech.* **199**, 569–593.

Longuet-Higgins, M. S. & Cokelet, E. D. 1976 The deformation of steep surface waves on water – I. A numerical method of computation. *Proc. R. Soc. Lond.* A **350**, 1–26.

Mei, C. C. 1986 Radiation of solitons by slender bodies advancing in a shallow channel. *J. Fluid Mech.* **162**, 53–67.

Nakos, D. E., Kring, D. C. & Sclavounos, P. D. 1993 Rankine panel methods for time-domain free surface flows. In *Proc. 6th Intl Conf. Numerical Ship Hydrodyn., University of Iowa* (ed. V. C. Patel & F. Stern), pp. 613–632. National Academy Press.

Orlanski, I. 1976 A simple boundary condition for unbounded hyperbolic flows. *J. Comput. Phys.* **21**, 251–269.

Pedersen, G. 1988 Three-dimensional wave patterns generated by moving disturbances at trans-critical speeds. *J. Fluid Mech.* **196**, 39–63.

Taha, T. R. & Ablowitz, M. J. 1984 Analytical and numerical aspects of certain nonlinear evolution equations: numerical Korteweg–de Vries equation. *J. Comput. Phys.* **55**, 231–253.

Thews, J. G. & Landweber, L. 1935 The influence of shallow water on the resistance of a cruiser model. *Tech. Rep.* 408. US Experimental Model Basin, Navy Yard, Washington, D.C.

Thews, J. G. & Landweber, L. 1936 A thirty-inch model of the S. S. Clairton in shallow water. *Tech. Rep.* 414. US Experimental Model Basin, Navy Yard, Washington, D.C.

Wehausen, J. V. & Laitone, E. V. 1960 *Surface Waves, Handbuch der Physik*, vol. 9, Springer.

Wu, D. M. & Wu, T. Y. 1982 Three dimensional nonlinear long waves due to moving surface pressure. In *Proc. 14th Symp. Naval Hydrodyn. Ann Arbor, Michigan*, pp. 103–129. National Academy Press.

Wu, T. Y. 1981 Long waves in ocean and coastal waters. *Proc. ASCE, J. Engng Mech. Div.* **107** (EM3), 501–522.

Wu, T. Y. 1987 Generation of upstream advancing solitons by moving disturbances. *J. Fluid Mech.* **184**, 75–99.

Zhang, D. H. & Chwang, A. T. 1999 On solitary waves forced by underwater moving objects. *J. Fluid Mech.* **389**, 119–135.